Intermetallic Ni_3Ga_1 catalyst for efficient ammonia reforming of light alkane

Siavash Fadaeerayeni,[1] Xingyi Lyu,[2] Lingzhe Fang,[2] Peng Wang,[3] Jiachun Wu,[1] Tao Li,[2,4*] Thomas Senftle,[3*] and Yizhi Xiang[1*]

[1] Dave C. Swalm School of Chemical Engineering, Mississippi State University; Mississippi State, Mississippi 39762, United States
[2] Department of Chemistry and Biochemistry, Northern Illinois University; DeKalb, Illinois 60115, United States
[3] Department of Chemical and Biomolecular Engineering, Rice University, Houston, Texas 77005, United States
[4] X-ray Science Division, Argonne National Laboratory; Lemont, Illinois 60439, United States

Abstract: Ammonia reforming of light alkane is conventionally employed for HCN production where co-product H_2 is burned for heating owing to the high reaction temperature (1200ºC) of such a highly endothermic process. Here we show that a Ni_3Ga_1 intermetallic compound (IMC) catalyst is highly efficient for such a reaction, realizing efficient conversion of C_1-C_3 alkanes at 575-750ºC. This makes it feasible for on-purpose CO_x-free H_2 production assuming that ammonia, as a H_2 carrier, is ubiquitously available from renewable energy. At 650 ºC and an alkane/ammonia ratio of 1/2, ethane and propane conversion of ~20% and methane conversion of 13% were obtained (with nearly 100% HCN selectivity for methane and ethane) over the unsupported Ni_3Ga_1 IMC, which also shows high stability under the investigated conditions due to the absence of coke deposition. This breakthrough is achieved by employing a stoichiometric Ni_3Ga_1 mixed oxalate solid solution as the precursor for the Ni_3Ga_1 IMC.

Introduction

The transformation of cheap and abundant light alkanes could have far-reaching implications in the chemical and energy sectors, yet remains a formidable challenge due to the lack of efficient catalysts/catalytic systems for the inert C-H and C-C bonds activation. While various catalytic processes, such as aromatization,[1-3] dehydrogenation,[4-7] partial oxidation,[8-11] and reforming,[12-14] have been extensively studied, so far, only steam methane reforming and propane dehydrogenation, have been employed for the large scale synthesis. Specifically, light alkane steam reforming is the main source of hydrogen (equation 1), which co-produces stoichiometric amounts of carbon oxide (CO and CO_2), imposing additional costs for CO transformation and CO_2 sequestration.

$$CH_4 + H_2O\ (l) \rightarrow CO + 3H_2 \qquad \Delta H = 250\ kJ/mol \qquad (1)$$

$$CH_4 + NH_3 \rightarrow HCN\ (g) + 3H_2 \qquad \Delta H = 256\ kJ/mol \qquad (2)$$

Light alkanes have also been utilized for HCN production through catalytic ammonia reforming (equation 2), known as Bläusaure aus Methan und Ammoniak (BMA) process in the industry. Such a process is highly energy intensive since it is performed at ultra-high temperatures (1200-1500 ºC) in alumina tube buddles coated with Pt as the catalyst.[15] While the BMA process co-produces >70% of H_2 (very similar to steam reforming from the reaction stoichiometry), it is economically uncompetitive for H_2 production because (i) the reaction temperature is significantly higher than steam reforming and (ii) the co-reactant NH_3 is currently still produced through Haber-Bosch process with H_2 from steam methane reforming. Consequently, H_2 from the BMA process is frequently used as fuel for heating the reactor in the current industry. Nonetheless, we believe

that such a reaction could be employed for CO_x-free H_2 production if the reaction can be realized at mild temperatures and green ammonia, as a H_2 carrier, is ubiquitously available from renewable energy.[16-17] Indeed, ammonia as a carbon-free H_2 carrier has been extensively recognized recently.[18-20] Considering that the market size of H_2 is larger than HCN, the catalytic hydrolysis ($HCN + H_2O \rightarrow NH_3 + CO$[21-23] or $NaCN + H_2O \rightarrow HCOONa + NH_3$[24-25]) can be employed to convert HCN back to NH_3. Although we understand HCN hydrolysis, currently it is not employed in industry and the process is of interest only for exhaust gas treatment.

Different from the BMA process, which requires ultra-high reaction temperature, our recent studies have shown that C_{2+} light alkanes, such as ethane and propane, can be transformed with ammonia into cyanides (CH_3CN or HCN) and H_2 over the metal modified HZSM-5 catalysts at 350-650 ºC.[16, 26-27] Such reactions were realized under anaerobic condition, which is different from the conventional ammoxidation.[28-29] Specifically, we found that the ammonia reforming (AmmoReform) of ethane and propane can be realized at 650 ºC over the isolated Re oxo anchored in HZSM-5 zeolite.[16] While the ReO_x/HZSM-5 catalyst is highly active and stable for the AmmoReform of C_{2+} alkanes, it is inactive for methane AmmoReform. Additionally, over the ReO_x/HZSM-5 catalyst, the reaction produces up to 20% of CH_3CN through the ammodehydrogenation mechanism,[26] decreasing H_2 selectivity.

In this paper, we report on the AmmoReform of C_1-C_3 alkanes for CO_x-free H_2 and HCN production at the same reaction temperature range for steam reforming. Different from the Lewis acid ReO_x/HZSM-5 catalyst, we show that the bimetallic Ni_3Ga_1 intermetallic compound (IMC) catalyst, in the absence of metal oxide as the support or dispersant, is highly active, selective (towards reforming instead of dehydrogenation), and stable (coke and sinter resistant) for the AmmoReform of methane, ethane, and propane, respectively. In particular, the structure of the fresh and used Ni_3Ga_1 IMC catalysts has been extensively characterized by in-situ/ex-situ synchrotron X-ray techniques. The structural transformation identified from the characterization results also is supported by *ab initio* thermodynamics calculations.

Results and discussion

Design, synthesis, and structural characterization of unsupported Ni_3Ga_1 IMC. The nanosized and unsupported Ni_3Ga_1 IMC catalyst was synthesized through co-precipitation of Ni^{2+} and Ga^{3+} cations with oxalate anion to create Ni_3Ga_1 mixed oxalate solid solution with a common framework structure,[30-31] which was followed by H_2-assisted thermal decomposition to form stoichiometric Ni_3Ga_1 IMC. A schematic illustration of the preparation procedure is shown in Figure 1a. Specifically, the Ni_3Ga_1 mixed oxalate was prepared through solvothermal coprecipitation from oxalic acid and nitrate precursors in isopropanol. TEM and STEM-EDS characterization of the oxalate (Figure 1f) shows the formation of an open framework structure with homogeneous distributions of Ni and Ga species, indicating that Ni^{2+} and Ga^{3+} cations were incorporated into a common oxalate framework structure. According to the XRD patterns, the binary Ni_3Ga_1 oxalate shows almost identical diffraction of the orthorhombic structure (Cccm space group) as the Ni oxalate dihydrate (see Figure S1 for XRD analysis of the oxalate

precursors), which suggested the incorporation of Ga^{3+} cation into the Ni oxalate dihydrate framework structure. The oxalate precursor was transformed into the unsupported Ni_3Ga_1 IMC catalyst by temperature-programmed decomposition (TPDec) under H_2. The TPDec profiles show the desorption of CO_2, CO, and CH_4 at temperatures between 200-400 ºC (Figure S2). The spectra of Ni_3Ga_1 oxalate show higher CO_2 peak temperature at 374 ºC than that for Ni and Ga oxalate at 365 and 321 ºC, respectively. Quantitative evaluation of the spectra based on "oxygen" balance suggested the formation of GaO_x (x<1) from the decomposition of monometallic Ga oxalate. Whereas, the binary Ni_3Ga_1 and monometallic Ni oxalate demonstrated the formation of metallic phases.

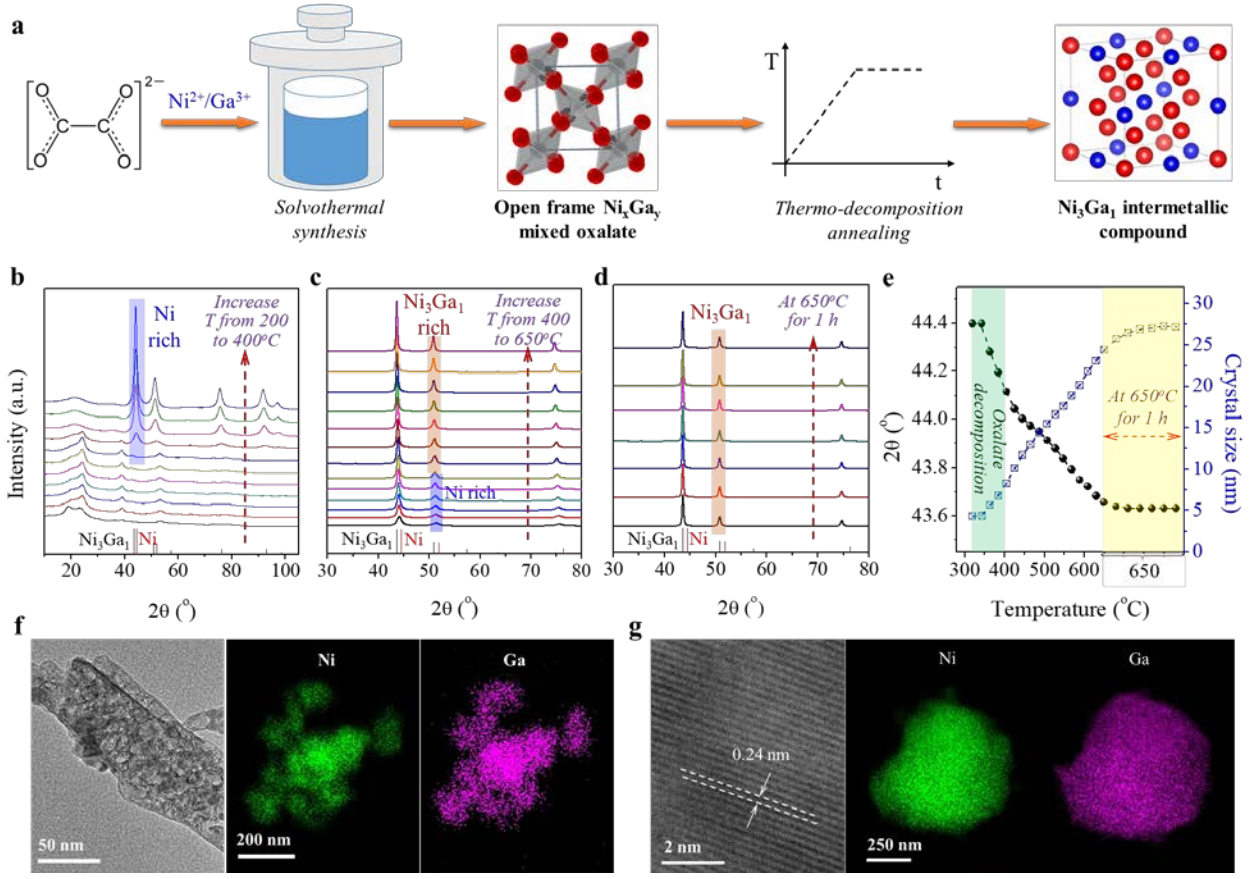

Figure 1. Preparation and characterization of unsupported Ni_3Ga_1 IMC nanoparticle. (a) schematic illustration of preparation procedure; (b)-(d) in-situ synchrotron XRD during temperature-programmed decomposition of oxalate precursor (see Figure S4 for zoomed XRD patterns); (e) evolution of crystal structure and size as a function of temperature during in-situ XRD; (f) TEM and STEM mapping of oxalate; (g) HRTEM and STEM-EDS of Ni_3Ga_1 IMC.

The structure evolution during the H_2-TPDec of Ni_3Ga_1 oxalate was investigated by in-situ synchrotron XRD (see Figure 1b-1d). As shown in Figure 1b, the Ni_3Ga_1 mixed oxalate starts decomposing at around 320 ºC (supported by the appearance of Ni diffraction peak at this temperature), which is consistent with the H_2-TPDec profiles shown in Figure S2. The diffraction of oxalate at temperatures between 200-320 ºC is different from the fresh Ni_3Ga_1 oxalate (Figure S1), indicating that the mixed oxalate was reconstructed after dehydration.[32] With the increase of

temperature from 320 to 400 ºC, the diffraction intensity related to Ni continuously increased, whereas the diffraction of Ga-related species was not identified, indicating that such species are highly dispersed or amorphous (see also Figure S3). The diffraction intensity continuously increased and the diffraction angle (2θ) decreased with increasing temperature from 400 to 650 ºC (see Figure 1c). The diffraction remains almost unchanged during annealing at 650 ºC for 1 h (see Figure 1d). More detailed dynamics of the crystal structure (shifting diffraction angle) and size (from Scherrer equation) during in-situ XRD based on the most intense diffraction peak of 111 plane are summarized in Figure 1e. It is seen that the diffraction angle shifted from 44.4º (for Ni) to 43.6º (for Ni_3Ga_1) with increasing temperature from 340 to 650 ºC (see Figure S4 for zoomed XRD patterns at 2θ between 40-56º), indicating that Ga species inserted into the Ni matrix, forming Ni_3Ga_1 IMC during the H_2-TPDec. The insertion of Ga to the Ni is fast during the oxalate decomposition process (at temperatures between 325 and 400 ºC, see Figure S2), then slows down during H_2 treatment until the temperature increases to 650 ºC. Accordingly, the crystal size increased almost linearly from 4.3 to 25 nm with increasing temperature from 340 to 650 ºC, indicating continuous crystallization during the process. The crystal size remains almost unchanged during the H_2 treatment at 650 ºC for 1 h. The HRTEM and STEM-EDS of the prepared Ni_3Ga_1 IMC can be found in Figure 1g. Noteworthily, both XRD and TEM show the formation of pure Ni_3Ga_1, other stoichiometries of Ni/Ga IMC and pure Ni were not identified.

Catalytic results. The catalytic data of the Ni_3Ga_1 IMC in the AmmoReform of methane, ethane, and propane are summarized in Figure 2 (a-c). It is seen that Ni_3Ga_1 is active for light alkane AmmoReform at temperatures > 575 ºC and the conversion increases with increasing reaction temperature (Figure 2a). Under the investigated temperatures, which are typical for light alkane steam or dry reforming, ethane and propane AmmoReform show similar conversion while methane AmmoReform shows lower conversion when compared at the same temperature. At 650 ºC, ethane and propane conversions are 20% and methane conversion is 13%. Ammonia conversion (Figure S5) during AmmoReform is slightly higher than light alkane, indicating that certain amounts of ammonia were decomposed to N_2 and H_2. In terms of carbon-based product selectivity, as shown in Figure 2b, methane AmmoReform produces 100% HCN and ethane AmmoReform shows decreased HCN selectivity at temperatures above 650 ºC. Whereas, propane AmmoReform shows 80-85% of HCN selectivity at temperatures below 675 ºC but decreased to 75% at 700 ºC. During the AmmoReform of C_{2+} light alkane, by-products such as CH_4, CH_3CN, and olefins can also be produced. Specifically, the formation of CH_4 according to hydrogenolysis ($C_2H_6 + H_2 \rightarrow 2CH_4$) and hydrogenation ($2HCN + 3H_2 \rightarrow 2CH_4 + N_2$) are favored at higher temperatures. Additionally, CH_3CN can be formed through AmmoDH as discussed in our previous paper.[26] For example, over the Re/HZSM-5 catalyst, the selectivity of HCN is only 75% (up to 20% of ethane was converted to CH_3CN).[16] With the Ni_3Ga_1 IMC catalyst, the selectivity of these by-products can be minimized at temperatures below 675 ºC for ethane AmmoReform. The rate of different product formation during the AmmoReform of ethane and propane can be found in Figures S6-S7, respectively.

While methane AmmoReform shows perfect carbon selectivity, ethane and propane AmmoReform outperform in terms of nitrogen-based selectivity. As shown in Figures S6-S8, the rate of N_2 formation (from ammonia decomposition) during methane AmmoReform is significantly higher than that during ethane and propane AmmoReform. The nitrogen-based HCN

selectivity (Figure S9) is around 80% during ethane and propane AmmoReform while is 60% at 750 ºC (decreased to 40% with decreasing temperature to 625 ºC) during methane AmmoReform. The nitrogen-based selectivity is a major concern during the commercial BMA process, the selectivity greater than 90% in methane AmmoReform was only found over the Pt catalyst at low ammonia partial pressure and high temperature.[33] According to the DFT calculations,[34] other transition metals such as Ni, Co, Rh, Ru, Ir, and Fe show relatively low selectivity. Nonetheless, the ammonia decomposition during the AmmoReform could further enhance H_2 production if H_2 is the target product and green ammonia is employed as an H_2 carrier. Figure 2c shows the rates of total H_2 formation as a function of light alkane conversion. It is seen that the rate of H_2 increases almost linearly with increasing conversion during methane and ethane AmmoReform, consistent with the high HCN selectivity discussed above. The different slopes of such linear behavior must be associated with the number of hydrogen atoms in the alkane molecule. However, such a linear relationship is absent for propane AmmoReform due to the formation of various by-products, which changes the stoichiometric ratio between produced H_2 and consumed alkane.

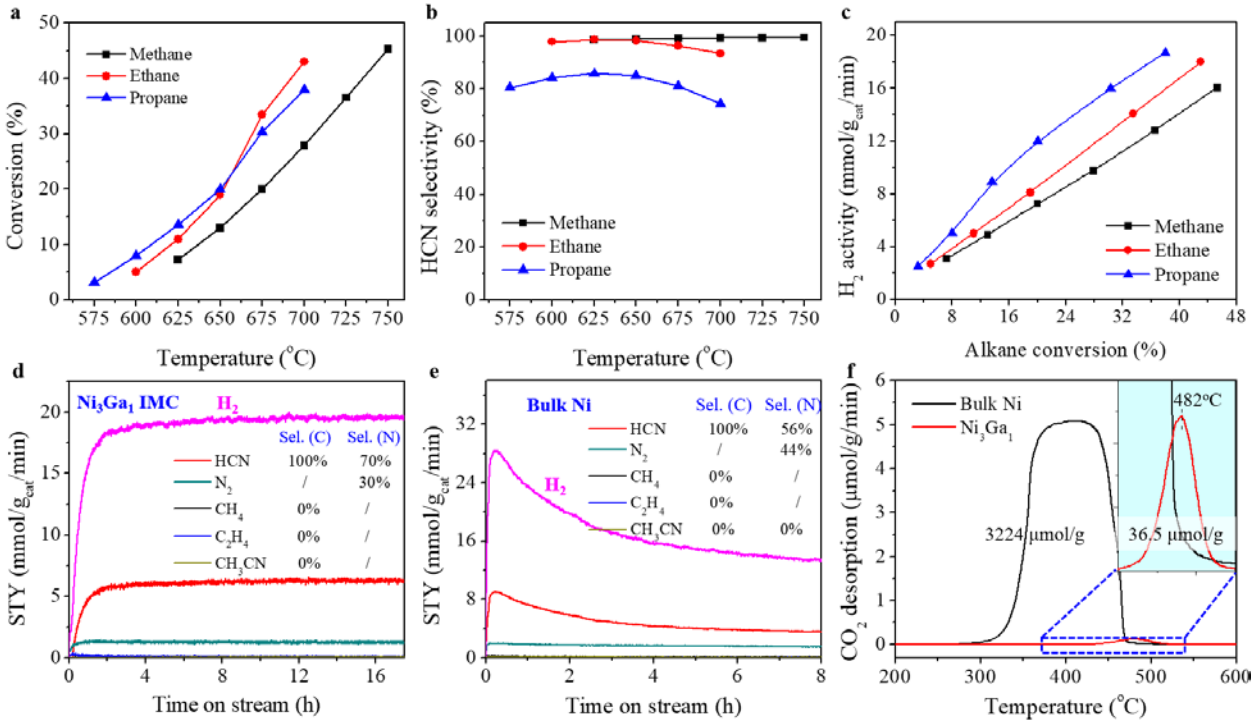

Figure 2. Catalytic data of light alkane ammonia reforming. (a)-(c) light alkanes conversion, HCN selectivity, and H_2 activity during AmmoReform of methane, ethane, and propane, respectively; (d) and (e): activity of various products during ethane AmmoReform over the Ni_3Ga_1 and bulk Ni catalysts, respectively; and (f) CO_2 desorption during the TPO of the used Ni_3Ga_1 and Ni catalysts. The reactions were carried out on 0.05 g of catalyst at 650 ºC, atmospheric pressure, the ratio of alkane/ammonia/Ar = 1/2/1, and space velocity of 800 mL/g_{cat}/min for (a)-(c) and 2400 mL/g_{cat}/min for (d)-(e). TPO was carried with 40 mL/min of 20% O_2/Ar and ramping at 10 ºC/min.

The stability (coke resistibility) of the Ni_3Ga_1 catalyst will be discussed based on ethane AmmoReform in contrast to the monometallic bulk Ni catalyst. Noteworthily, the monometallic Ga catalyst is inactive for light alkane AmmoReform. As shown in Figure 2d, the Ni_3Ga_1 catalyst

shows outstanding stability during ethane AmmoReform at 650 ºC and a space velocity of 2400 $mL/g_{cat}/min$. No deactivation was observed for rates of H_2 and HCN, as well as ethane conversion and HCN selectivity (Figure S10a) with a time-on-stream of 17 h. An independent stability test at a space velocity of 800 $mL/g_{cat}/min$ shows stable ethane conversion up to 70 h (Figure S10b). The same ultrahigh stability was also found for methane AmmoReform (Figure S11). Unlike the Ni_3Ga_1 catalyst, the monometallic Ni although active for ethane AmmoReform, the rates of H_2 and HCN attenuate significantly with time-on-stream (Figure 2e). While the initial rate of H_2 is up to 28 mmol/g/min, it decreased to < 14 mmol/g/min after 8 h. The fast deactivation of the Ni catalyst must be associated with coke deposition from ethane cracking on the Ni particles.[35] As shown in Figure 2f, the total carbon deposition on the Ni catalyst is up to 3224 μmol/g according to the TPO, which can be oxidized to CO_2 at temperatures of 300-500 ºC. Although the Ni_3Ga_1 catalyst is highly stable during ethane AmmoReform, small amounts of CO_2 (~36.5 μmol/g) were desorbed during the TPO at a higher temperature of 482 ºC. We advocate that such CO_2 originate from the oxidation of the C that penetrated into the Ni_3Ga_1 lattice rather than coke as in the case of the Ni catalyst.

Catalytically active structure during AmmoReform. The Ni_3Ga_1 IMC catalyst after the ethane AmmoReform has been extensively characterized by the ex-situ XRD and X-ray atomic pair distribution function (PDF) to identify the structural transformation during the reaction process. As shown in Figure 3a, the diffraction of Ni_3Ga_1 shifted towards lower angles (from 43.6 to 43.3º) after the reaction, indicating the partial dissolution of C into the Ni_3Ga_1 lattice.[36] As carbon atoms penetrated into the octahedral interstices of the Ni_3Ga_1, the lattice parameter increased from 0.3587 to around 0.362 nm according to Portnoi et al.[36] Consequently, shifting the diffraction peak to lower 2θ, and all of the peaks in the PDF of used Ni_3Ga_1 (see Figure 3b) slightly shifted toward higher r-distance after the reaction. Noteworthily, the PDF of the fresh Ni_3Ga_1 sample fits well with the Ni_3Ga_1 IMC (Figure S12). While the shift of both XRD and PDF peaks strongly suggests the C dissolution in the used catalyst, the Ni-C atomic pairs were not identified from the PDF.

Further characterization of the fresh and used Ni_3Ga_1 catalyst by X-ray absorption spectroscopy at Ni K-edge is shown in Figures 3c and 3d. The X-ray absorption near-edge structure (XANES) spectra of fresh and used Ni_3Ga_1 catalyst are almost identical, which show a pre-edge peak at around 8333 eV (originated from 1s→3d transition) as the Ni and Ni foil, indicating that the oxidation state was not changed after the reaction despite the partial dissolution of C atoms into the Ni_3Ga_1 interstices. The Fourier transform of the extended X-ray absorption fine structure (EXAFS) spectrum of the used Ni_3Ga_1 catalyst shifted slightly towards higher R (from 2.21 to 2.23 Å) in contrast to the fresh Ni_3Ga_1, which is consistent with the XRD and PDF results. The pronounced peaks at R distance slightly above 2.2 Å for the Ni_3Ga_1 samples originated from the Ni-Ni and Ni-Ga scattering.[37-38] In contrast, the Ni-Ni scattering in the Ni and Ni foil show a peak at R-distance below 2.19 Å, once again confirming the formation of Ni_3Ga_1 IMC in the bimetallic samples. The same as the PDF results, the Ni-C scattering was not clearly identified from the EXAFS spectrum of the used Ni_3Ga_1 catalyst, although the small peak at 1.65 Å can be possibly assigned to it. We advocate that the C dissolution into the Ni_3Ga_1 lattice is rather negligible according to the PDF and EXAFS, demonstrating high stability of the N_3Ga_1 IMC during the

AmmoReform reaction. Indeed, from the CO_2 desorbed during the TPO process, the atomic ratio of Ni/C is up to around 330/1.

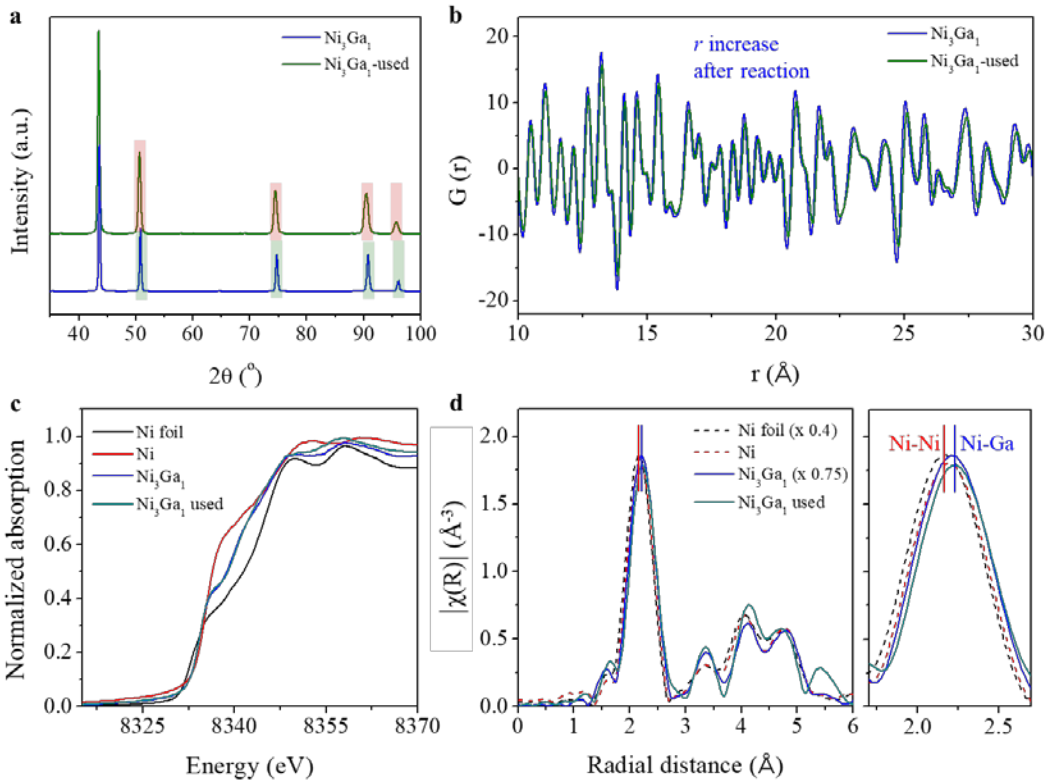

Figure 3. X-ray characterizations of fresh and used Ni_3Ga_1 catalyst. (a) ex-situ XRD; (b) X-ray atomic pair distribution function (PDF); (c) Ni K-edge normalized XANES spectra and and (d) Fourier transformed EXAFS spectrum.

Ab initio thermodynamics methods (see SI for computational details) were employed to further understand the phase transition and carbonization process of Ni_3Ga_1 during the AmmoReform reaction at 650 °C. Specifically, the free energy of carbon (μ_C) during AmmoReform was calculated as a function of the H_2 and C_2H_6 partial pressure, based on which relevant phase boundaries were identified (see Figure 4, each line represents a constant free energy of carbon). The phase transitions at each boundary are illustrated on the right side in Figure 4. The solid line (μ_C = -8.21 eV) and dotted line (μ_C = -7.88 eV) represent the phase transition between surface adsorption of carbon from zero (clean surface) to 1/3 coverage and from 1/3 coverage to carbon-carbon dimer formation, respectively (see Figure S13-S14). The dashed line (μ_C = -8.40 eV) represents the bulk transition between Ni_3Ga_1 and Ni_3Ga_1C, which was identified by comparing the free energies of the bulk phases. The induction period (green arrow) during ethane AmmoReform passes through three different phase regions. During the initial reaction (red circle), carbon deposition is favored (atomic carbons can adsorb on the Ni_3Ga_1 surfaces and migrate into the subsurface which leads to Ni_3Ga_1C or coke formation). As the reaction progresses through the induction period, the partial pressure of H_2 increases while that of C_2H_6 decreases (see Figure S15). Consequently, the deposited carbon on the Ni_3Ga_1 favors the formation of Ni_3Ga_1C rather than coke. The partial pressure of H_2 and C_2H_6 during steady-state ethane AmmoReform is located in

the Ni_3Ga_1 region. Therefore, under AmmoReform conditions, the Ni_3Ga_1 IMC is expected to be the dominant phase in the used catalyst, which is consistent with the characterization results.

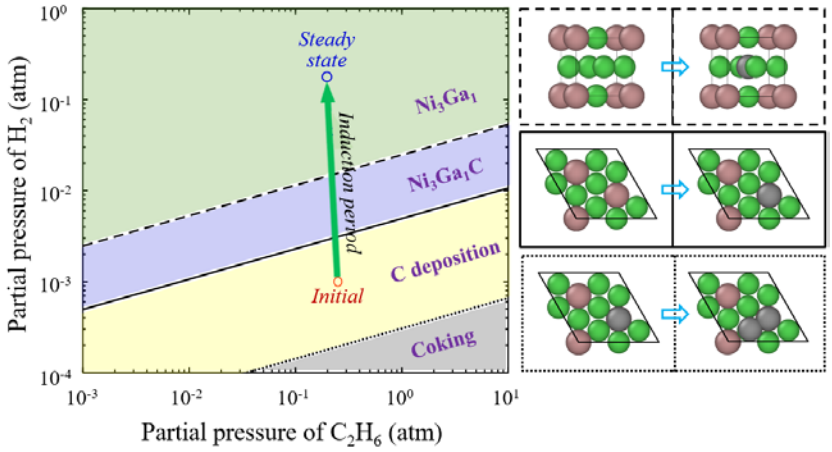

Figure 4. The phase transition (as a function of H_2 and C_2H_6 partial pressure) during ethane AmmoReform at 650 °C. Each line represents a particular boundary between two phases as shown in the three panels on the right. Dashed line: Ni_3Ga_1 and Ni_3Ga_1C boundary. Solid line: the boundary between clean Ni_3Ga_1 (111) and 1/3 coverage of carbon. Dotted line: the boundary between 1/3 coverage of carbon and 2/3 coverage of carbon (dimer formation). Red and blue circles represent the H_2 and C_2H_6 partial pressure during the induction period and steady-state, respectively.

Discussion. Characterization of the used catalyst by the synchrotron X-ray techniques in combination with the *Ab initio* thermodynamic calculations led us to conclude that the IMC is an efficient new group of catalysts for the AmmoReform. The Ni_3Ga_1 IMC has been identified as a promising catalyst for CO_2 hydrogenation[39] and light alkane conversion through dehydrogenation[40] and dry reforming[37] due to the improved activity and stability. According to Norskov and coworkers, the Ni-Ga IMC shows an optimal binding strength of the oxygen intermediate during CO_2 hydrogenation.[39] Quite similarly, during the CO_2 reforming of CH_4, Lee and coworkers found that the Ni_3Ga_1 and $Ni_3Ga_1C_{0.25}$ IMCs require less energy than Ni for the oxidation of C^* to CO^*.[37] In this study, we suggest that the CH_x^* (from the light alkane dehydrogenation and cracking) will react with the NH_x^* intermediate, forming CNH_x^* as the precursor of HCN. Specifically, under the steady-state AmmoReform conditions, deep dehydrogenation of CH_x^* to form C^* is not favored due to the high H_2 partial pressure. Therefore, the Ni_3Ga_1 shows outstanding coke resistibility during the AmmoReform of light alkanes.

The Ni center of the Ni_3Ga_1 IMC is the catalytically active site for the AmmoReform since the monometallic Ga catalyst is totally inactive. The Ni_3Ga_1 catalyst was also prepared through the precipitation of carbonate (see Figure S1 for the XRD pattern), however, the catalyst is inactive for ethane AmmoReform. Additionally, the Ni_3Ga_1/Al_2O_3 (prepared through incipient wetness impregnation) was also tested for comparison purposes. While the catalyst is active for ethane AmmoReform, it deactivates significantly like the case of monometallic Ni catalyst (Figure S16), indicating the failed formation of the stoichiometric Ni_3Ga_1 IMC using the impregnation method with Al_2O_3 as the support. According to Laursen et al.,[40] off-stoichiometric Ni_3Ga_1 was formed with a Ni_1Ga_1/Al_2O_3 catalyst, where excess Ga was trapped on the oxide surface and left unincorporated into the IMC particles. Therefore, the oxalate method, due to the formation of Ni-Ga solution with atomic scale mixing of Ni^{2+} and Ga^{3+} cations, is essential for the formation of

unsupported stoichiometric Ni_3Ga_1 IMC from its precursor. Moreover, Ni_1Ga_1 catalyst was also prepared using the oxalate method and tested for ethane AmmoReform. Despite the Ni_1Ga_1 oxalate precursor being employed, the Ni_3Ga_1 IMC was produced after H_2-TPDec. The Ni_1Ga_1 catalyst shows slightly higher activity than the Ni_3Ga_1 catalyst due to the decreased crystal size (excess gallium species serve as a dispersant). More detailed studies about the influence of the Ni/Ga ratio (in the oxalate precursor) on the structure and catalytic performance are ongoing.

Conclusion

Ni_3/Ga_1 mixed oxalate with a common framework structure was synthesized through solvothermal co-precipitation of Ni^{2+} and Ga^{3+} cations with oxalate anion. Such a mixed oxalate solid solution can be transformed into Ni_3Ga_1 (with the same stoichiometric ratio as the precursor) IMC through H_2-assisted thermal decomposition. The nanosized and unsupported IMC is an ideal model catalyst (in the absence of metal/support interactions) for understanding the intrinsic activity behavior of the Ni_3Ga_1 in catalytic reactions. We show here that such a Ni_3Ga_1 IMC catalyst is highly active, selective, and stable in light alkane AmmoReform, which was conventionally realized using a Pt-based catalyst at temperatures up to 1200ºC for HCN production. Specifically, efficient AmmoReform of C_1-C_3 alkanes can be achieved at 575-750ºC (reaction temperature is the same as the steam-/dry reforming). Ethane and propane conversion of ~20% and methane conversion of 13% were obtained at 650 ºC. Due to the decreased reaction temperature, such a reaction might be employed for on-purpose CO_x-free H_2 production assuming that ammonia, as a H_2 carrier, is ubiquitously available from renewable energy. Moreover, the structure of the fresh and used Ni_3Ga_1 IMC catalysts has been extensively characterized by in-situ/ex-situ synchrotron X-ray techniques, including XRD, XAS, and PDF. The characterization results suggested that while C might penetrated into the octahedral interstices of the Ni_3Ga_1, such C dissolution shows negligible influence on the stability of the Ni_3Ga_1 IMC. The favorability of such structural transformation is also supported by the *ab initio* thermodynamics calculations.

ASSOCIATED CONTENT

Supporting Information.

Experimental details (catalyst preparation, catalytic performance evaluation, catalyst characterization, and computational methods), XRD patterns of the oxalate precursor, H2-TPDec profiles, ex situ XRD patterns of Ni, Ni_3Ga_1, and Ga_2O_3, zoomed XRD patterns, additional catalytic data, and additional computational data. This material is available free of charge via the Internet at http://pubs.acs.org.

AUTHOR INFORMATION

Corresponding Author

tsenftle@rice.edu (TS); tli4@niu.edu (TL); yzxiang@che.msstate.edu (YX)

Notes

The authors declare no conflict of interest.

Acknowledgments

Y.X. and T.L. are grateful for the financial support from the National Science Foundation (#2210760 and # 2210868) for this project. This research used resources of the Advanced Photon Source, a U.S. Department of Energy (DOE) Office of Science User Facility operated for the DOE Office of Science by Argonne National Laboratory under Contract No. AC02-06CH11357. Electron microscopy works were done at the Institute for Imaging and Analytical Technologies (I2AT) at Mississippi State University [supported by the National Science Foundation (MRI-1126743)].

Reference

1. Guo, X.; Fang, G.; Li, G.; Ma, H.; Fan, H.; Yu, L.; Ma, C.; Wu, X.; Deng, D.; Wei, M.; Tan, D.; Si, R.; Zhang, S.; Li, J.; Sun, L.; Tang, Z.; Pan, X.; Bao, X., Direct, Nonoxidative Conversion of Methane to Ethylene, Aromatics, and Hydrogen. *Science* **2014,** *344* (6184), 616-619.
2. Gao, J.; Zheng, Y.; Jehng, J.-M.; Tang, Y.; Wachs, I. E.; Podkolzin, S. G., Identification of molybdenum oxide nanostructures on zeolites for natural gas conversion. *Science* **2015,** *348* (6235), 686-690.
3. Chen, G.; Fang, L.; Li, T.; Xiang, Y., Ultralow-Loading Pt/Zn Hybrid Cluster in Zeolite HZSM-5 for Efficient Dehydroaromatization. *J. Am. Chem. Soc.* **2022,** *144* (26), 11831-11839.
4. Liu, L.; Lopez-Haro, M.; Lopes, C. W.; Li, C.; Concepcion, P.; Simonelli, L.; Calvino, J. J.; Corma, A., Regioselective generation and reactivity control of subnanometric platinum clusters in zeolites for high-temperature catalysis. *Nat. Mater.* **2019,** *18* (8), 866-873.
5. Liu, L.; Lopez-Haro, M.; Lopes, C. W.; Rojas-Buzo, S.; Concepcion, P.; Manzorro, R.; Simonelli, L.; Sattler, A.; Serna, P.; Calvino, J. J.; Corma, A., Structural modulation and direct measurement of subnanometric bimetallic PtSn clusters confined in zeolites. *Nat. Catal.* **2020,** *3* (8), 628-638.
6. Ryoo, R.; Kim, J.; Jo, C.; Han, S. W.; Kim, J.-C.; Park, H.; Han, J.; Shin, H. S.; Shin, J. W., Rare-earth–platinum alloy nanoparticles in mesoporous zeolite for catalysis. *Nature* **2020,** *585* (7824), 221-224.
7. Xie, Z.; Tian, D.; Xie, M.; Yang, S.-Z.; Xu, Y.; Rui, N.; Lee, J. H.; Senanayake, S. D.; Li, K.; Wang, H.; Kattel, S.; Chen, J. G., Interfacial Active Sites for CO_2 Assisted Selective Cleavage of C–C/C–H Bonds in Ethane. *Chem* **2020,** *6* (10), 2703-2716.
8. Shan, J.; Li, M.; Allard, L. F.; Lee, S.; Flytzani-Stephanopoulos, M., Mild oxidation of methane to methanol or acetic acid on supported isolated rhodium catalysts. *Nature* **2017,** *551* (7682), 605-608.
9. Sushkevich, V. L.; Palagin, D.; Ranocchiari, M.; van Bokhoven, J. A., Selective anaerobic oxidation of methane enables direct synthesis of methanol. *Science* **2017,** *356* (6337), 523-527.
10. Tomkins, P.; Ranocchiari, M.; van Bokhoven, J. A., Direct Conversion of Methane to Methanol under Mild Conditions over Cu-Zeolites and beyond. *Acc. Chem. Res.* **2017,** *50* (2), 418-425.
11. Ravi, M.; Sushkevich, V. L.; Knorpp, A. J.; Newton, M. A.; Palagin, D.; Pinar, A. B.; Ranocchiari, M.; van Bokhoven, J. A., Misconceptions and challenges in methane-to-methanol over transition-metal-exchanged zeolites. *Nat. Catal.* **2019,** *2* (6), 485-494.
12. Buelens, L. C.; Galvita, V. V.; Poelman, H.; Detavernier, C.; Marin, G. B., Super-dry reforming of methane intensifies CO_2 utilization via Le Chatelier's principle. *Science* **2016,** *354* (6311), 449-452.
13. Palmer, C.; Upham, D. C.; Smart, S.; Gordon, M. J.; Metiu, H.; McFarland, E. W., Dry reforming of methane catalysed by molten metal alloys. *Nat. Catal.* **2020,** *3* (1), 83-89.

14. Song, Y.; Ozdemir, E.; Ramesh, S.; Adishev, A.; Subramanian, S.; Harale, A.; Albuali, M.; Fadhel, B. A.; Jamal, A.; Moon, D.; Choi, S. H.; Yavuz, C. T., Dry reforming of methane by stable Ni–Mo nanocatalysts on single-crystalline MgO. *Science* **2020,** *367* (6479), 777-781.
15. Endter, F., Die technische Synthese von Cyanwasserstoff aus Methan und Ammoniak ohne Zusatz von Sauerstoff. *Chem. Ing. Techn.* **1958,** *30* (5), 305-310.
16. Fadaeerayeni, S.; Yu, X.; Sarnello, E.; Bao, Z.; Jiang, X.; Unocic, R. R.; Fang, L.; Wu, Z.; Li, T.; Xiang, Y., Ammonia-Assisted Light Alkane Anti-coke Reforming on Isolated ReOx Sites in Zeolite. *ACS Catal.* **2022,** *12* (5), 3165-3172.
17. Xiang, Y., Ammonia-assisted reforming and dehydrogenation toward efficient light alkane conversion. *Green Chem.* **2023,** *25* (20), 7904-7915.
18. Schüth, F.; Palkovits, R.; Schlögl, R.; Su, D. S., Ammonia as a possible element in an energy infrastructure: catalysts for ammonia decomposition. *Energy Environ. Sci.* **2012,** *5* (4), 6278-6289.
19. Service, R. F. Ammonia—a renewable fuel made from sun, air, and water—could power the globe without carbon. https://www.science.org/content/article/ammonia-renewable-fuel-made-sun-air-and-water-could-power-globe-without-carbon (accessed 2023-12-29), doi: 10.1126/science.aau7489
20. MacFarlane, D. R.; Cherepanov, P. V.; Choi, J.; Suryanto, B. H. R.; Hodgetts, R. Y.; Bakker, J. M.; Ferrero Vallana, F. M.; Simonov, A. N., A Roadmap to the Ammonia Economy. *Joule* **2020,** *4* (6), 1186-1205.
21. Kröcher, O.; Elsener, M., Hydrolysis and oxidation of gaseous HCN over heterogeneous catalysts. *Appl. Catal. B* **2009,** *92* (1), 75-89.
22. Yan, L.; Tian, S.; Zhou, J.; Yuan, X., Catalytic hydrolysis of gaseous HCN over Cu–Ni/γ-Al_2O_3 catalyst: parameters and conditions. *Front. Environ. Sci. Eng.* **2016,** *10* (6), 5.
23. Song, Z.; Zhang, Q.; Ning, P.; Wang, Y.; Duan, Y.; Wang, J.; Huang, Z., Catalytic hydrolysis of HCN on ZSM-5 modified by Fe or Nb for HCN removal: surface species and performance. *RSC Adv.* **2016,** *6* (112), 111389-111397.
24. Heise, G. W.; Foote, H. E., The Production of Ammonia and Formates from Cyanides, Ferrocyanides, and Cyanized Briquets. *J. Ind. Eng. Chem.* **1920,** *12* (4), 331-336.
25. Sulzer, H., Verfahren zur Darstellung von Ammoniak und Ameisensäure aus Kalkstickstoff. *Angew. Chem.* **1912,** *25*, 1268-1273.
26. Chen, G.; Liang, T.; Yoo, P.; Fadaeerayeni, S.; Sarnello, E.; Li, T.; Liao, P.; Xiang, Y., Catalytic Light Alkanes Conversion through Anaerobic Ammodehydrogenation. *ACS Catal.* **2021,** *11* (13), 7987-7995.
27. Chen, G.; Fadaeerayeni, S.; Fang, L.; Sarnello, E.; Li, T.; Toghiani, H.; Xiang, Y., Acetonitrile formation from ethane or ethylene through anaerobic ammodehydrogenation. *Catal. Today* **2023,** *416*, 113751.
28. Liu, X.; Liang, T.; Barbosa, R.; Chen, G.; Toghiani, H.; Xiang, Y., Ammoxidation of Ethane to Acetonitrile and Ethylene: Reaction Transient Analysis for the Co/HZSM-5 Catalyst. *ACS Omega* **2020,** *5* (3), 1669-1678.
29. Liang, T.; Liu, X.; He, Y.; Barbosa, R.; Chen, G.; Fan, W.; Xiang, Y., Highly selective Sn/HZSM-5 catalyst for ethane ammoxidation to acetonitrile and ethylene. *Appl. Catal. A* **2021,** *610*, 117942.
30. Xiang, Y.; Chitry, V.; Liddicoat, P.; Felfer, P.; Cairney, J.; Ringer, S.; Kruse, N., Long-Chain Terminal Alcohols through Catalytic CO Hydrogenation. *J. Am. Chem. Soc.* **2013,** *135* (19), 7114-7117.
31. Xiang, Y.; Kruse, N., Tuning the catalytic CO hydrogenation to straight- and long-chain aldehydes/alcohols and olefins/paraffins. *Nat. Commun.* **2016,** *7*, 13058.

32. Puzan, A. N.; Baumer, V. N.; Lisovytskiy, D. V.; Mateychenko, P. V., Structure transformations in nickel oxalate dihydrate $NiC_2O_4 \cdot 2H_2O$ and nickel formate dihydrate $Ni(HCO_2)_2 \cdot 2H_2O$ during thermal decomposition. *J. Solid State Chem.* **2018,** *266*, 133-142.
33. Hasenberg, D.; Schmidt, L. D., HCN synthesis from CH_4 and NH_3 on clean Rh. *J. Catal.* **1985,** *91* (1), 116-131.
34. Grabow, L. C.; Studt, F.; Abild-Pedersen, F.; Petzold, V.; Kleis, J.; Bligaard, T.; Nørskov, J. K., Descriptor-Based Analysis Applied to HCN Synthesis from NH_3 and CH_4. *Angew. Chem. Int. Ed.* **2011,** *50* (20), 4601-4605.
35. Fadaeerayeni, S.; Shan, J.; Sarnello, E.; Xu, H.; Wang, H.; Cheng, J.; Li, T.; Toghiani, H.; Xiang, Y., Nickel/gallium modified HZSM-5 for ethane aromatization: Influence of metal function on reactivity and stability. *Appl. Catal. A* **2020,** *601*, 117629.
36. Portnoi, V. K.; Leonov, A. V.; Fedotov, S. A., Ordering in mechanically alloyed Ni(Ga) and Ni(Ga, C) solid solutions during heating. *Phys. Met. Metallogr.* **2009,** *107* (3), 276-284.
37. Kim, K. Y.; Lee, J. H.; Lee, H.; Noh, W. Y.; Kim, E. H.; Ra, E. C.; Kim, S. K.; An, K.; Lee, J. S., Layered Double Hydroxide-Derived Intermetallic $Ni_3GaC_{0.25}$ Catalysts for Dry Reforming of Methane. *ACS Catal.* **2021**, 11091-11102.
38. Hu, M.; Yang, W.; Liu, S.; Zhu, W.; Li, Y.; Hu, B.; Chen, Z.; Shen, R.; Cheong, W.-C.; Wang, Y.; Zhou, K.; Peng, Q.; Chen, C.; Li, Y., Topological self-template directed synthesis of multi-shelled intermetallic Ni_3Ga hollow microspheres for the selective hydrogenation of alkyne. *Chem. Sci.* **2019,** *10* (2), 614-619.
39. Studt, F.; Sharafutdinov, I.; Abild-Pedersen, F.; Elkjaer, C. F.; Hummelshoj, J. S.; Dahl, S.; Chorkendorff, I.; Norskov, J. K., Discovery of a Ni-Ga catalyst for carbon dioxide reduction to methanol. *Nat. Chem.* **2014,** *6* (4), 320-324.
40. He, Y.; Song, Y.; Cullen, D. A.; Laursen, S., Selective and Stable Non-Noble-Metal Intermetallic Compound Catalyst for the Direct Dehydrogenation of Propane to Propylene. *J. Am. Chem. Soc.* **2018,** *140* (43), 14010-14014.

TOC Graphic

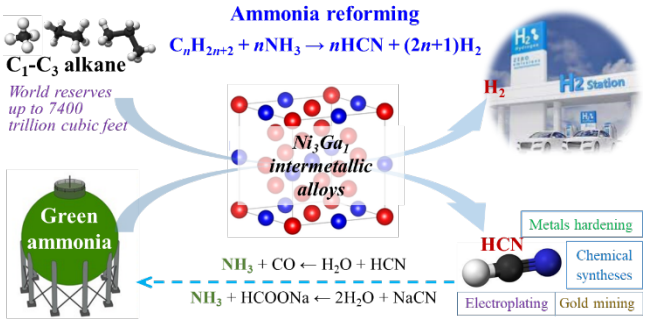
Ammonia reforming
$C_nH_{2n+2} + nNH_3 \rightarrow nHCN + (2n+1)H_2$
C_1-C_3 alkane
World reserves up to 7400 trillion cubic feet
Ni_3Ga_1 intermetallic alloys
H_2
Green ammonia
HCN
Metals hardening
Chemical syntheses
Electroplating
Gold mining
$NH_3 + CO \leftarrow H_2O + HCN$
$NH_3 + HCOONa \leftarrow 2H_2O + NaCN$